Minerals Engineering 157 (2020) 106535

Contents lists available at ScienceDirect

Minerals Engineering

journal homepage: www.elsevier.com/locate/mineng

Recycling mica and carbonate-rich mine tailings in alkali-activated composites: A synergy with metakaolin

He Niu[a], Mariam Abdulkareem[b], Harisankar Sreenivasan[a], Anu M. Kantola[c], Jouni Havukainen[b], Mika Horttanainen[b], Ville-Veikko Telkki[c], Paivo Kinnunen[a,*], Mirja Illikainen[a]

[a] Fibre and Particle Engineering Research Unit, University of Oulu, P.O. Box 4300, FI-90570 Oulu, Finland
[b] Lappeenranta-Lahti University of Technology, School of Energy Systems, Department of Sustainability Science, P.O. Box 20, FI-53851 Lappeenranta, Finland
[c] NMR Research Unit, Faculty of Science, University of Oulu, P.O. Box 3000, FI-90014 Oulu, Finland

ARTICLE INFO

Keywords:
Mine tailings
Metakaolin
Geopolymers
Gel chemistry
Life cycle assessment
Zeolite
Mechanochemical activation

ABSTRACT

The main objective of this paper was to investigate the alkali activation of mine tailings (MT) after mechanochemical activation and the effect of metakaolin (MK) addition. Finnish mica-rich tailings from a phosphate mine were studied as precursors for alkali-activated materials (AAM) with a potential application as a substitute for ordinary Portland cement (OPC). The principal physical properties (water absorption, apparent porosity and unconfined compressive strength) were measured for samples containing 30% to 70% tailings. Zeolite phases such as natrolite and cancrinite were observed and the formation of C-(N)-A-S-H[1] and N-A-S-H gels was identified by XRD, DRIFT, FESEM-EDS and NMR technologies. A life cycle assessment (LCA) was conducted on specimens in comparison to OPC. This work indicated that phosphate MT can be recycled through alkali activation with lower CO_2 emission compared to all-metakaolin geopolymers and that the binder phase formed at the most promising tailings contents (60– 70%) was C-(N)-A-S-H gel.

1. Introduction

Greenhouse gas emissions are a global issue and the leading cause of the global climate change. One tonne of Portland cement manufactured produces approximately one tonne of carbon dioxide (Hasanbeigi et al., 2010). Therefore, developing materials with lower CO_2 emission as alternative to the traditional Portland cement is important. Alkali-activated materials (AAM) are cementitious binders that have been investigated for several decades with respect to their excellent performances and mechanical properties, refractory, and acid resistance (Bakharev, 2005; Duxson et al., 2007; Novais et al., 2018; Vickers et al., 2015). AAM can contribute to reduce the carbon footprint, especially when waste materials, such as fly ash, slag, waste rocks and mine tailings are utilised (Kinnunen et al., 2018; MacKenzie et al., 2007; Maragkos et al., 2009; Rattanasak and Chindaprasirt, 2009).

AAM are produced from solid precursors under alkaline conditions, which involves both a high-calcium system and low-calcium system (geopolymer), containing C-(A)-S-H gel and N-A-S-H gel, respectively (Provis, 2013). Moreover, the coexistence of both cementitious binder gels; that is, C-(N)-A-S-H is possible. (Yip et al., 2005) The compatibility of C-S-H and N-A-S-H systems has been found to be highly susceptible to the threshold value of OH^- concentration, which also influences the gel formation sequences (Alonso and Palomo, 2001a; Alonso and Palomo, 2001b). Calcium addition has also been used to modify the N-A-S-H gels, forming (N,C)-A-S-H gels under high pH conditions (> 12) (García-Lodeiro et al., 2010). The product phase of sodium-silicate activation of Ca-containing aluminosilicate precursors consists of amorphous C-A-S-H gel along with C-(N)-A-S-H gel (Myers et al., 2015).

MT are currently underutilised industrial side streams, with potential to be used as a secondary raw material in AAM. The usual disposal of phosphate MT is done by transporting them to storage impoundments (Kauppila et al., 2013). The storage of tailings poses an environmental risk and cost money and energy for construction and maintenance. Therefore, the reprocessing and remediation of mining waste is an interesting alternative. The Siilinjärvi phosphate MT (Eastern Finland) consists of 65% phlogopite mica (2:1-layer lattice aluminosilicate) in addition to carbonates, silicates and apatite (O'Brien et al., 2015). It cannot be directly used for alkali activation due to its poor chemical reactivity. Furthermore, the gel formation of MT-based geopolymer is a complex issue as it depends on the specific minerals presenting in the tailings and has been little explored so far. Since MT are not highly reactive precursors, they have been mostly used in

* Corresponding author.
E-mail address: Paivo.Kinnunen@oulu.fi (P. Kinnunen).
[1] C-CaO, N-Na_2O, A-Al_2O_3, S-SiO_2, H-H_2O.

https://doi.org/10.1016/j.mineng.2020.106535
Received 30 March 2020; Received in revised form 11 June 2020; Accepted 29 June 2020
Available online 12 August 2020
0892-6875/

conjunction with reactive raw materials, such as metallurgical slag. Thermal analysis was successfully conducted on the tailings-slag geopolymers, indicating both C-S-H and C-A-S-H gels decomposition and recrystallisation (Ye et al., 2014a). Zhang et al. (Zhang, 2013) summarised that waste materials such as hematite tailings, gold MT, copper MT can be used for producing geopolymer bricks, among which the coexistence of $CaCO_3$ and N-A-S-H gel systems was achieved by introducing cement kiln dust for alkali activation (Ahmari and Zhang, 2013). These studies shed the light on the gel formation in tailings-based geopolymers and on how to guide the gel development in tailings-based geopolymers.

Pre-treatment is often necessary for MT before utilisation. S. Moukannaa et al. (Moukannaa et al., 2019, 2018) studied the heat treatment and alkaline fusion on phosphate MT, and they also investigated the alkali activation of such pre-treated tailings with fly ash and MK. Although that study carried out the recycling of phosphate MT, which consisted mainly of fluorapatite and quartz, and therefore the findings are not relevant to the utilisation of mica and carbonate-rich side streams in our study. In addition, high-temperature pre-treatments can be energy and time consuming compared to mechanochemical treatment, which is a more efficient and greener method (Boldyreva, 2013). Mechanochemical activation, especially intensive grinding, can generate internal stress, induced by shear force and impact between particles and grinding media. In our previous research, the amorphisation of phlogopite-bearing phosphate MT by mechanochemical activation was observed (Niu et al., 2020). Alkaline reactivity tests demonstrated that mechanochemical activation improved reactivity seen as increased silicon and aluminium dissolution rates in alkaline media. Mechanochemical activation has been conducted on different precursors, such as kaolin (Balczár et al., 2016), fly ash (Mucsi et al., 2015), natural minerals (MacKenzie et al., 2007) and vanadium MT (Wei et al., 2017) for the purpose of alkali activation; however, the effect of mechanochemical activation on mica-rich phosphate MT has not been studied.

Therefore, the aim of this work was to alkali-activate mechanochemical activated phosphate MT with various tailings/MK mass ratios and to investigate the mechanism of gel formation in this complex multi-mineral system. Thus, it might be possible to guide the utilisation of mine tailings as secondary materials for construction and building application. Life cycle assessment of the end-products was conducted and compared to similar construction materials based on ordinary Portland cement (OPC).

2. Materials and methods

The metakaolin (MK; MetaMax, Aquaminerals Finland Ltd) was purchased from BASF (Germany) and the phosphate MT were obtained from Siilinjärvi phosphate mining site (yearly production:10 Mt/a; Stock: 280 Mt), Finland, which mainly consists of phlogopite (64%), dolomite (6%), calcite (14%) and tremolite (1.4%). The chemical compositions of both MK and MT are provided in

Table 1. The sodium hydroxide (VWR Chemicals, > 97%) and sodium silicate solution (VWR Chemicals, SiO_2: 26.8%, Na_2O: 8.2%) were used as alkali activator. Twelve M NaOH solution was prepared before experiments and left overnight to cool down.

The MT were subjected to mechanochemical activation (Vibratory disc mill; Retsch RS 200) before alkali-activation according to our previous research. It indicated that 4-min ground raw tailings obtained a D50 of 7.22 μm and a BET surface area of 6.9745 ± 0.0210 m^2/g. In addition, it also generated around 40% of amorphous phase according to Rietveld refinement. The X-ray diffraction and DRIFT were also conducted on both precursors as provided in Fig. A1. The typical DRIFT bands of MK are shown in Fig. A1a, after which Table 1 provides the positions and assigned bands of MT. It should be noted that the shift of dolomite and calcite bands is significantly attributed to the pre-treatment and the Mg/Ca ratio in the initial composition. For instance, the bands in the range of 2600 to 2500 cm^{-1} can be assigned to the combination of ν_1 and ν_2 modes, which is in line with the previous studies (Gunasekaran and Anbalagan, n.d.; Nguyen et al., 1991). The morphologies of MK and mechanically activated MT are shown in Fig. A2 using scanning electron microscope (FESEM, Zeiss). The particle shape of MT is normally irregular as MK.

Table 2
Experimental mix design for alkali-activated materials.*

Sample name	PMT (Phosphate tailings)/wt %	MK (Metakaolin)/ wt%	H_2O/Na	Na/Al	Si/Al	Liquid/ solid
PM 0/10	0	100	4.31	0.59	1.31	0.45
PM 1/9	10	90	4.29	0.65	1.39	0.45
PM 2/8	20	80	4.07	0.72	1.49	0.45
PM 3/7	30	70	3.70	0.8	1.62	0.35
PM 4/6	40	60	3.69	0.9	1.77	0.35
PM 5/5	50	50	3.67	1.03	1.97	0.35
PM 6/4	60	40	3.65	1.2	2.24	0.35
PM 7/3	70	30	3.64	1.44	2.60	0.35
PM 8/2	80	20	2.54	1.79	3.14	0.3
PM 9/1	90	10	2.53	2.37	4.03	0.3
PM 10/0	100	0	4.07	3.47	5.72	0.40

* The calculated ratios are based on the assumption of fully reacted reactants.

2.1. Preparation of alkali-activated samples

The alkali-activation was subjected to the binary mixture of mechanochemically activated phosphate MT and MK. The mix design is given in Table 2. The mass ratio of sodium silicate solution and sodium hydroxide solution was fixed at 1.4 for all samples, which is based on the PM 5/5 where Na/Al and Si/Al ratios are 1 and 2 respectively. The liquid to solid ratio was variable due to the rheological properties of the slurry; however, the samples named through PM 3/7 to PM 7/3 had a constant liquid/solid mass ratio of 0.35. It requires a higher liquid/solid ratio from PM 0/10 to PM 2/8, while a lower ratio was applied for PM 8/2 to PM 9/1. Two precursors were dry-mixed for 5 min before alkali-activation. The slurry was thoroughly blended by a high shear mixer at 1000 rpm for 5 min; thereafter, it was shaped by using Polyethylene moulds with dimensions of 20 mm in height and 25 mm in diameter. The vibrating machine (Vortex-Genie 2, Prolab Oy) was used to remove all air bubbles. The samples were demoulded after curing at 40 °C for 24 h and then continuously cured in a sealed plastic bag for 7 days.

2.2. Sample characterisation

Physical properties, such as apparent porosity and water absorption were tested according to the standard EN-1936: 2006 (EN, 2007). After the preliminary UCS test of all the samples, subsequent

Table 1
Chemical composition of the raw materials by XRF analysis.

Sample	SiO_2	Al_2O_3	CaO	MgO	K_2O	Fe_2O_3	P_2O_5	TiO_2	MnO	Others	L.O.I.
PMT	32.99	7.09	12.92	17.27	5.53	7.99	0.95	0.27	0.12	0.86	14.01
MK	53	44.5	–	–	0.1	0.4	–	1.4	–	–	0.3

characterisations were conducted on five samples in particular through PM 3/7 to PM 7/3, since they were synthesised under the same L/S ratio. The 7-day cured samples were crushed into pieces and mounted for scanning electron microscopy (SEM). Apart from the SEM analysis, the fragments were ground manually using pestle and mortar and submerged in isopropanol to remove the loosely bound water, thereby ceasing the alkali activation. The resulted powders were subsequently stored in a desiccator until measurement.

X-ray diffraction analysis was subjected to a Rigaku SmartLab 4.5 kW, with the equipment parameters of Co source (40 kV and 135 mA) K_α ($K_{\alpha1}$ = 1.78892 Å; $K_{\alpha2}$ = 1.79278 Å; $K_{\alpha1}/K_{\alpha2}$ = 0.5), scan rate of 3°/min and 0.02°/step. The phase identification was conducted using the PDXL2 Software Suite with integrated PDF-4 (2019) database. Chemical characterisation of hardened samples was performed by using diffuse reflectance infrared Fourier transform (DRIFT). The spectra were collected using a Bruker Vertex 80v spectrometer (USA) with a range of 400 to 4,000 cm^{-1}, and 40 scans were taken at a resolution of 1 cm^{-1} for each sample. The morphology of AAM was characterised with Zeiss ULTRA plus FESEM, with an acceleration voltage of 5 kV. FESEM-EDS (Energy Dispersive X-ray Spectroscopy) analysis was conducted using FESEM with an acceleration voltage of 15 kV and beam current of 120 × 10^{-8} A. The polished cross-sections of PM samples were subjected to at least 50 points analysis under the magnification of ×3000 and the working distance was 6 to 8 mm. UCS was performed with the Zwick Roell 100 kN machine with a loading force of 3 mm/min until failure. Soaking tests were performed by immersing three hardened samples in deionised water (DI-water) for 24 h with a sample/water mass ratio of 1/3 for each batch, after which the liquid and the solid were subjected to the inductively coupled plasma-optical emission spectroscopy (ICP-OES) and UCS, respectively.

The ^{27}Al and ^{29}Si NMR spectra were obtained on a Bruker Advance III 300 spectrometer operating at 78.24 MHz for ^{27}Al and 59.65 MHz for ^{29}Si. For the purpose of conducting MAS experiments, the samples were packed into 7 mm zirconia rotors, then rotated with a frequency of 7 kHz. For ^{27}Al, 2048 scans were accumulated with a repetition rate of 2 s, and for ^{29}Si the corresponding parameters were 8192 scans and 3 s. Neither proton decoupling nor cross polarisation was used. The chemical shifts were referenced to $Al(NO_3)_3$ and TMS (tetramethylsilane), for which the reference shifts were set to zero ppm.

2.3. Life cycle assessment (LCA)

LCA is a method for assessing and evaluating potential environmental impacts of a product or system. It is performed in four phases: (1) goal and scope definition, (2) inventory phase, (3) impact assessment phase, and (4) interpretation phase (EN ISO 14040, 2006). This method has been applied in assessing the environmental impacts of numerous materials, including AAM (Abdulkareem et al., 2019; Passuello et al., 2017; Petrillo et al., 2016). The goal of the study is to estimate and compare impacts generated from developing alkali-activated binder from phosphate MT and MK in comparison to OPC. The study framework considers the four processes of cradle-to-gate alkali-activated binder formulations, including raw material production, waste beneficiation, mixing of constituents and associated emissions and energy consumptions. The functional unit is the production of 1 kg of binder. Excluded processes from this study include transportation as it is assumed all raw materials considered in this study are locally produced and have similar transportation distances. The use phase and end-of-life phase are also excluded from this study as it is assumed that comparable and similar impacts are expected from these phases.

The LCA study was performed using the Centrum voor Milieukunde Leiden (CML) 2016 method (Thinkstep, 2019). CML 2016 indicators provide information on the environmental issues associated with inputs and outputs of the product system (EN ISO 14040, 2006). This assessment principally focuses on global warming potential (GWP), acidification potential (AP), eutrophication potential (EP) and abiotic depletion potential (ADP fossil) impact categories. These impact categories are relevant for assessment of emissions generated during the production of binders (Chen et al., 2010a, Van Den Heede and De Belie, 2012), which is the central issue of this study. Moreover, the characterisation method for these impacts are better established than for the toxicity impacts, where both lack of reliable data and methodological uncertainty reduce their reliability (Merrild et al., 2012). The LCA modelling was performed using the GaBi LCA modelling software (version 8.6.0.20).

2.4. Life cycle inventory

Life cycle inventory (LCI) is the phase where all unit processes included in the system boundary are quantified. LCI data of the different processes considered in this study are listed in Appendix B. Data sources for Life cycle inventory Table B1. The data were collected from GaBi database, scientific literature and environmental reports from industrial organisations. Unit processes such as sodium hydroxide, water and electricity were sourced from the GaBi database. The unit process of sodium silicate solution was modelled following the approach and LCI data from (Fawer et al., 1999). This solution is produced by dissolving sodium silicate lumps in water at an elevated temperature and pressure to yield a solution with 37% of total solids which is thereafter filtered (Fawer et al., 1999). Data for energy production were adapted to the Finnish context, and geographical scope of this study was limited to Finland, thus, a Finnish dataset was used. Where dataset for Finland is unavailable, the EU-28 dataset was used. For the baseline study, CEM I as reported by (CEMBUREAU, 2015) was used as a basis of comparison. It composed about 92.5% clinker as main constituent and minor additional constituents. Environmental impacts of capital goods such as trucks, equipment, buildings were not taken into account in this study.

Oven curing is required for alkali-activated binder during production is essential for initiating chemical reaction of the binder at first instance. The energy consumed during curing in the lab was 1.87 MJ/kg at 40°C for 24 h. Mixing of the ingredients consumed 0.0045 MJ/kg and grinding of phosphate tailings consumed 1.25 MJ/kg in the lab. Kaolin as reported from the GaBi database was already dried and milled. However, to produce metakaolin, kaolin had to be calcined, consuming 2.5 MJ/kg of natural gas (Heath et al., 2014; NLK, 2002). The synthesis conditions for the alkali-activated binders are defined at laboratory scale. Thus, energy consumption is lower when full scale commercially tested technology is used.

3. Results and discussion

3.1. Physical properties

The 7-day UCS of alkali-activated binders are shown in Fig. 1a. The variation of MK amount had a profound impact on the mechanical properties of tailings-metakaolin based geopolymers. It should be noted that the mix design here is not optimal for the alkali-activation of MK, thereby the solely MK-based geopolymer obtained a rather low UCS. With lower amounts of substitution of MK by MT from 0% to 30%, the UCS of each sample does not change considerably. When the proportion of MT continuously increases, the growth of UCS can be seen until it reaches 70%, at which point it gains the highest UCS of more than 20 MPa. Thereafter, the UCS diminishes with the incremental MT content. The mix design of samples containing 30–70% MT was otherwise identical; therefore, the following characterisations were conducted on these specimens. The samples were specially dubbed as 'PM samples' in the following part of this article. Fig. 1b demonstrates the variation of PM samples for water absorption and apparent porosity. It is obvious that apparent porosity and water absorption substantially decreased from PM 6/4 to PM 7/3, indicating the formation of highly dense binder regarding to the Si/Al ratio close to 2.6. The apparent porosity has a good correlation with their strength results; that is, the

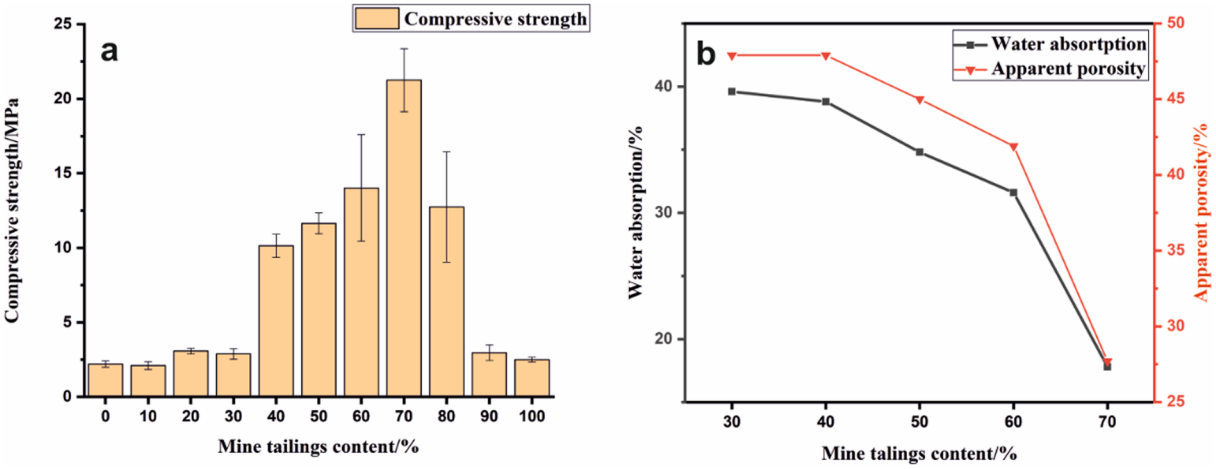

Fig. 1. (a) Compressive strength of tailings-metakaolin based geopolymers after 7 days of curing, (b) water absorption and apparent porosity of tailings-metakaolin based geopolymers after 7 days of curing.

increasing UCS varies with decreasing apparent porosity and water absorption. Since the mould has a fractionally thinner dimension, the measured compressive strength might be slightly lower than the genuine one.

3.2. XRD and DRIFT

The diffractograms of PM samples are presented in Fig. 2, in which XRD intensity was normalised by the strongest reflection of each sample in order to compare the relative intensities. The main crystalline phases of PM samples originate from MT, of which the mineralogical components include phlogopite (ICDD, PDF-4 #04-012-5381), calcite (ICDD, PDF-4 #04-012-0489), dolomite (ICDD, PDF-4 #04-015-9848), and tremolite (ICDD, PDF-4 #04-013-2249). A new phase conspicuously appeared in PM 3/7, PM 4/6 and PM 5/5 according to XRD pattern, which is ascribed to the reflection of vermiculite (ICDD, PDF-4 #04-017-7291). Vermiculite is structurally analogous to phlogopite and has both balanced cations (Mg^{2+}, Ca^{2+} and Na^{+}) and water filling its interlayer. It should be mentioned that the K^{+} becomes loosely bonded in the interlayer during mechanochemical activation. Thus, this transformation results from the cation exchange by smaller Na^{+} during the alkali activation. The formation of vermiculite can be seen from PM 3/7 to PM 5/5, whilst it disappears once zeolite such as natrolite was formed. It is possible to conclude that vermiculite might be the intermediate phase in favour of the generation of zeolites, that is, zeolitisation of vermiculite (Johnson and Worrall, 2007). The peak of quartz at around 29°/2θ corresponds to the trend of decreasing amount of raw metakaolin from PM 3/7 to PM 7/3. A new carbonate mineral, gaylussite, was formed by reacting amorphised MT (containing intermediate calcium of 14.75%) with alkali activator in PM 5/5. As for PM 6/4, a crystalline zeolite, natrolite, appeared alkali activation. Another crystalline phase, cancrinite, shows in the XRD pattern of PM 7/3, nucleating from gels and acting as the microaggregates embedded in the binder matrix (Ye et al., 2014b).

Fig. 3 shows DRIFT spectra of tailings-metakaolin based geopolymers, in which the band alternations prove the occurrence of geopolymerisation. The partial disappearance of in-plane vibration in Al–O–Si band at 665 cm^{-1} (see Table A1) indicates the decomposition of tetrahedral layers in amorphous phlogopite and suggested that mechanochemical activated MT participated in the alkali activation. In addition, the weakened band at 720 cm^{-1} of MK during alkali activation is assigned to symmetric Al–O–Si stretching vibration (Mo et al., 2014). The frequency at 780 to 790 cm^{-1} appearing demonstrated the quartz in the original MK (Fernández-Jiménez and Palomo, 2005). The original Si–O–T band of MK in the region of 1300 cm^{-1} no longer existed in any of the PM samples due to the dissolution in alkali activator; therefore, the new band appeared at 1200 cm^{-1} in PM 3/7, representing the Si–OH stretching vibrations in the resulting geopolymers (Mo et al., 2014). Furthermore, this band (dash line) progressively shifted to a lower frequency with the incremental content of MT,

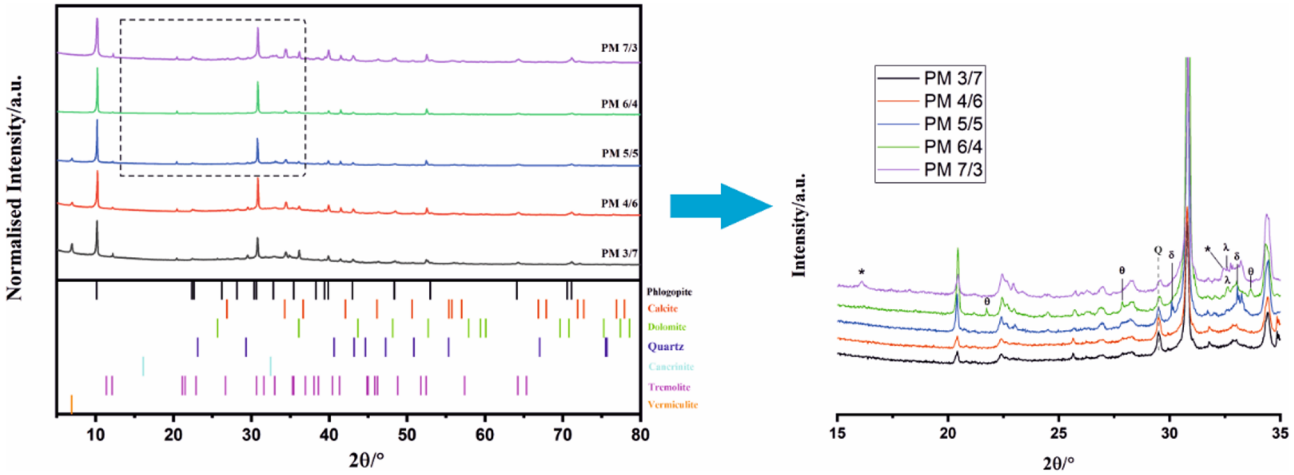

Fig. 2. X-ray diffraction patterns of tailings-metakaolin based geopolymer samples. δ: gaylussite (PDF# 04-010-3621); θ: natrolite (PDF#04-011-7181); λ: sodium calcium carbonate (PDF#04-02102551); *: cancrinite (PDF#04-015-7815); Q: Quartz (PDF#04-007-2627).

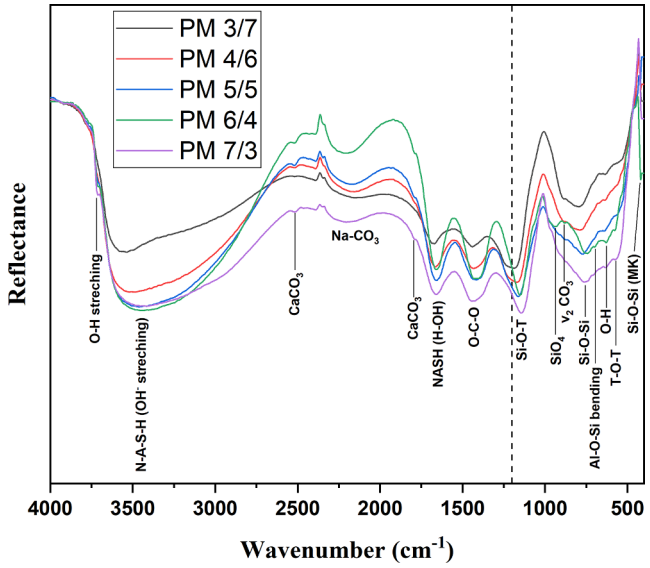

Fig. 3. DRIFT spectra of the tailings-metakaolin based geopolymer samples.

showing that more polycondensation occurred. Another evidence is the bending band of Si–O shifting to a lower frequencies (700 cm^{-1}), which was also characterised as the formation of geopolymers (Palomo and Glasser, 1992). Two distinct broad bands were situated at approximately 3450 cm^{-1} and 1650 cm^{-1}, representing the O–H stretching band and O–H bending band, respectively, which indicates the occurrence of polycondensation (Chindaprasirt et al., 2009). It is interesting that the sharpest O–H stretching (3711 cm^{-1}) for the trioctahedral group ($Mg_3(OH)$) practically disappeared, compared to that of raw tailings (see Table A1). This observation can be interpreted to mean that the crystal phlogopite degradation likely occurred during the alkali activation. The presence of the band at approximately 1460 cm^{-1} in all PM samples has been ascribed to sodium carbonate (Gadsden, 1975). Another significant band between 2000 to 2200 cm^{-1} was assigned to the stretching vibration of the functional group of Na_2CO_3; that is, carbonate minerals, generated by reacting alkali activator with amorphous MT (Bouaissi, 2019). The hint of the formation of cancrinite can be found by the following assignments: 879 cm^{-1} for C-O bend (CO_3^{2-}) and 1400 cm^{-1} for C–O stretch (CO_3^{2-}), which is in line with the results of previous studies (Król et al., 2018; Mozgawa, 2001; Ye et al., 2014b). Once combined with the results of XRD, the study indicated that there was no crystalline cancrinite in PM 6/4, and the new carbonate mineral was assigned to sodium calcium carbonate (Fig. 2). Furthermore, the weak bands at 736 cm^{-1} and 759 cm^{-1} could be attributed to the formation of T-O bonds in the interconnected tetrahedra in PM 6/4. The formation of single four ring (S4R) was in accordance with the previous study which stated that the band range of 720–760 cm^{-1} is assigned to the formation of natrolite zeolite (four-membered rings) (Fernández-Jiménez and Palomo, 2005; Mozgawa, 2001). The new peak appeared at 760 cm^{-1} in the spectrum of PM 7/3 which is assigned to v_4 Si-O which was found in other blended gel system of C-S-H and N-A-S-H (García-Lodeiro et al., 2008).

3.3. SEM and EDS

The transformation from phlogopite into vermiculite was observed in PM 3/7 and PM 4/6 (Fig. 4), in which the morphology resembled the light weight aggregates (expanded vermiculite) implanted in cement matrix (Mladenovič et al., 2004). The formation of vermiculite partially resulted from the expended interlayer of phlogopite by mechanochemical activation; however, it differed from the vermiculite with Mg^{2+} and H_2O filling in interlayers (Smith Aitken, 1965). Since the mechanochemically activated MT can release more K^+ ions during the alkaline activation, it can be replaced by smaller Na^+ ions by cation exchange forming Na^+–H_2O interlayers. From the morphology of PM 3/7, original particles are entrained in the matrix suggesting a lack of dissolution in PM 3/7. While dissolved particles from MT generate more binder gels in PM 4/6 (fewer original particles compared to PM 3/7), it can be postulated that the polycondensation practically stopped after MK dissolution. The Si/Al ratio for PM 3/7 and PM 4/6 was 1.62 and 1.77, respectively. According to the research by Oelkers et al. (Oelkers and Gislason, 2001), easily dissolved aluminate units can be adsorbed on reactant surfaces, thereby decreasing the dissolution of silicate units. This unbalanced dissolution leads to a lack of formation of geopolymeric linkages. Accompanied with large residues of unreacted MT, the resulting materials exhibits rather poor mechanical strength.

The gel morphology of PM 5/5 exhibited distinctly different features compared with PM 3/7 and PM 4/6, where the calcium-rich gel, sodium-deficient matrix (light grey), displayed a clear boundary with the sodium-rich (darker grey) one according to the elemental mappings (Fig. 5). The calcium-rich gel had unreacted calcite (i.e. crystalline calcite) particles embedded, in which amorphous calcite was the source of calcium for the generation of C-A-S-H binder. When alkali activators were introduced, amorphous calcite can react with sodium hydroxide, generating calcium species $Ca(OH)_2$ (neutral) and $Na_2Ca(CO_3)_2{\cdot}5H_2O$ (gaylussite) (Valentini et al., 2018). The presence of gaylussite was confirmed by using XRD and DRIFT analyses (Fig. 2 and Fig. 3). The monomeric units of Si and Al tetrahedra were dissolved from MK into alkaline activator, forming N-A-S-H and C-(N)-A-S-H gels. Ca-rich species are prone to react with Ca-bearing species; thereafter, reaction with Si and Al species occurs. Thus, this phenomenon explains how amorphous calcite dissolution favours the generation of C-(N)-A-S-H binder, whilst Na-rich regions displayed pronounced propensity towards N-A-S-H gel. Additionally, at which alkaline concentration is higher than 10 M, the N-A-S-H gel becomes the main product, whilst C-S-H gel is the secondary phase when calcium hydroxide exists (Alonso and Palomo, 2001a). Consequently, amorphous carbonate minerals (calcite, dolomite) can react with the alkaline activator to generate more dissolved calcium ions; these calcium ions are incorporated in amorphous alkaline aluminosilicate hydrates. The dissolution of calcium ions led to the formation of a halo in the Ca mapping around the crystalline calcite particles. It can be interpreted that the boundary between the two gels formed a gaylussite ring (bright green in the Ca map), which resulted from the high aqueous pH in N-A-S-H gel impeding the dissolution of Ca cation. This gaylussite ring prevented the interaction between C-(N)-A-S-H and N-A-S-H gels, decreasing the compatibility of these gels which in turn led to undesirable mechanical properties.

The scanning electron miscroscopy (SEM) image of PM 6/4 (Fig. 6) reveals the crystallisation of the zeolite phase among gel binders. The main substances, natrolite and C-(N)-A-S-H phases, formed in the final product after alkali activation. The bundles of fibres or fan-like crystals in PM 6/4 have been ascribed to the formation of natrolite zeolite, which was produced by breaking the T-O bonds of chemically reactive precursors and regeopolymerisation (Huang et al., 2016; Slaty et al., 2015). The energy dispersive spectra of these two phases are provided in Fig. 6 (P1 and P2). The nucleation of natrolite has been hypothesised as arising from the presence of NaOH, MK, activated MT and the curing conditions as depicted below (El Hafid and Hajjaji, 2015).

$$\mathit{Precursors\ (calcite,\ dolomite)} + \mathit{Alkali\ activator} \xrightarrow{\mathit{initial\ stage},40\,^{\circ}C} \mathit{Gaylussite} + \mathit{Aluminosilicate\ species} \xrightarrow{\mathit{final\ stage},40\,^{\circ}C} \mathit{Natrolite} + C-(N)-A-S-H$$

There is some evidence to suggest that natrolite is likely formed on the vermiculite where the reflections of vermiculite vanished in XRD pattern (Fig. 2). Therefore, it is reasonable to assume that the natrolite crystallised from the aluminosilicate tetrahedral layers with the supplementation of MK and alkali activator.

In the image of PM 7/3, the tailings-metakaolin based geopolymers

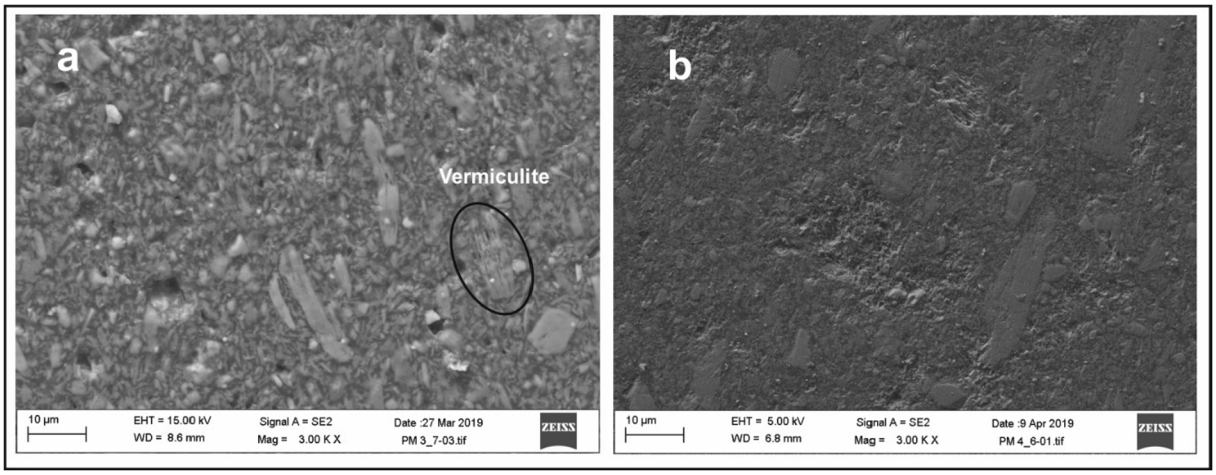

Fig. 4. SEM images of a) PM 3/7 and b) PM 4/6.

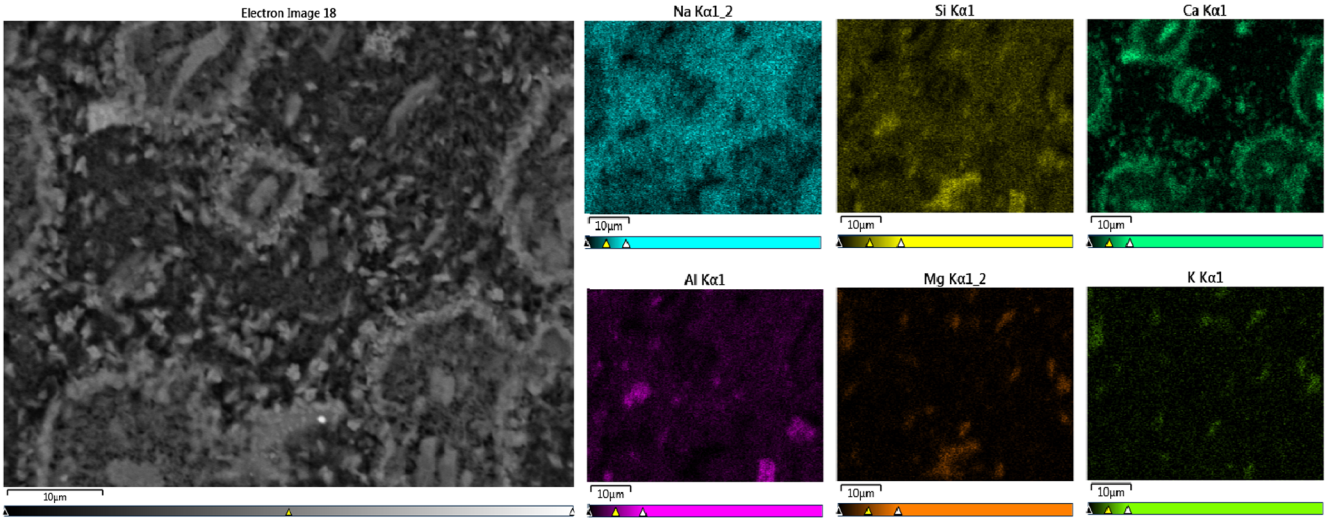

Fig. 5. FESEM back-scattered electron (BSE) images and elemental maps for the PM 5/5.

consisted of densely geopolymeric matrix (Fig. 7). The Mg- and K-bearing particles in mapping images represented unreacted MT (phlogopite) due to its poor alkali reactivity and structural stability. This result is also in line with its lowest apparent porosity. It should be noted that the formation of zeolite-like products results from the alkalinity and composition of raw materials (Criado et al., 2007). Unlike chemically reactive raw materials (calcinated materials), the inert MT precursor must be first pre-treated in order to supply more soluble aluminosilicate phases. In this work, the pre-treatment was still insufficient for the alkali activation, unless the supplement of MK for the inadequate aluminium content in phosphate MT. The morphology in the SEM image contained column-shaped grains, which has been assigned to the formation of C-(N)-A-S-H phase (Chen et al., 2010b). The generation of C-(N)-A-S-H gel is believed to occur at the expense of N-A-S-H phase through the ion exchange mechanism; in addition, PM 7/3 possessed the highest calcium content. This phenomenon was ascribed to the assumption proposed by I. Garcia-Lodeiro (Garcia-Lodeiro et al., 2011). Nevertheless, it slightly differed from this case regarding to the effect of pH, as the pH was 12.67 (> 12) for PM 7/3. The existence of C-(N)-A-S-H was confirmed, which meant that the formation of such gel is depended on not only the ion exchange mechanism but also the alkaline reaction between carbonate minerals (tailings) and MK. Furthermore, it can be hypothesised that the formation of cancrinite is ascribed to the recrystallization from C-(N)-A-S-H gel; however, crystalline cancrinite was not observed in the SEM images probably due to its scale and the complex matrix of C-(N)-A-S-H gel. From the perspective of UCS, PM 7/3 presents a promising UCS compared to other PM samples. Poor mechanical properties have been attributed to the amount of crystalline phase in the resulting samples, in which gel-to-crystal transformation leads to the reduction of mechanical strength due to the occurrence of open porosity and microcracking occurring in this course (Palomo and Glasser, 1992).

The minerology of MT generates complex compositions in the AAM as displayed in the ternary diagrams (Fig. 8). The raw tailings barely contained sodium content, whereas it was rich in calcium. Additionally, the MT had a wider cluster in the $CaO\text{-}Al_2O_3\text{-}SiO_2$ diagram, which is due to calcium-containing minerals such as calcite and dolomite. Thus, the data of raw tailings are not taken into account during chemical analysis in this section. The $Na_2O\text{-}Al_2O_3\text{-}SiO_2$ diagram displayed more clustered EDS data points than those in the $CaO\text{-}Al_2O_3\text{-}SiO_2$ counterpart. PM 3/7 exhibited no correlation with geopolymeric gel formation in both diagrams, thereby showing rather weak UCS. However, PM 4/6 and PM 5/5 generated N-A-S-H and Na-rich C-(N)-A-S-H gel after alkali activation, illustrating the increase of UCS which almost doubled that of PM 3/7. N-A-S-H gel predominantly formed in the $Na_2O\text{-}Al_2O_3\text{-}SiO_2$ system of PM 5/5; these results were consistent with the observation in SEM. The data points of PM 6/4 located in the N-A-S-H gel area which are genuinely assigned to the natrolite, and the Na-rich C-(N)-A-S-H gel which has confirmed in preceding results. With MT content increased to 70%, it promotes the formation of C-(N)-A-S-H gel and the (re)

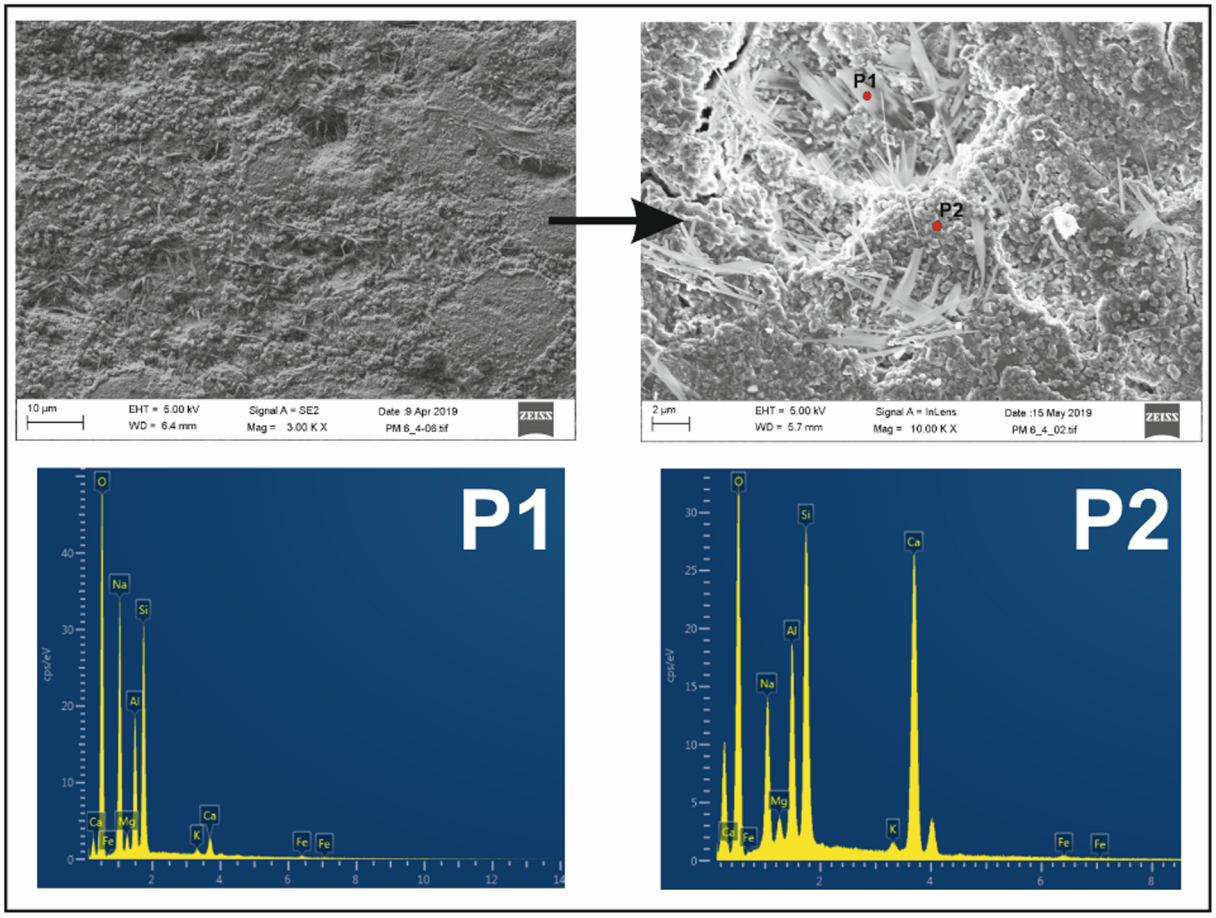

Fig. 6. SEM micrographs of PM 6/4 and energy dispersive spactra of fibrous phase (P1) and gel matrix (P2).

crystallisation of cancrinite is developed. Compared with PM 7/3, PM 5/5 and PM 6/4 predominantly consisted of Na-rich C-(N)-A-S-H gel.

The ternary diagram explicitly illustrated the development of gel formation with the increasing tailings content. At a lower content of sodium ions (Na/Al less than 1), the accumulation of free alumina units occurred, thereby preventing further polycondensation. With the incremental Na/Al ratio, it facilitated the alkali activation; thereafter, it produced not only N-A-S-H gel but also C-(N)-A-S-H gel after the appearance of sodium calcium carbonate and calcium hydroxide.

3.4. ^{29}Si and ^{27}Al MAS NMR

The results of the NMR analysis are shown in Fig. 9. Among all the products, analysis was performed for three samples: PM 3/7, PM 5/5 and PM 7/3 (which have low, medium and high compressive strength, respectively). Among all the reactants, measurements were done only for MK. Measurement of MT was unsuccessful due to its high iron content.

The results of the ^{29}Si NMR analysis are depicted in Fig. 9a. The

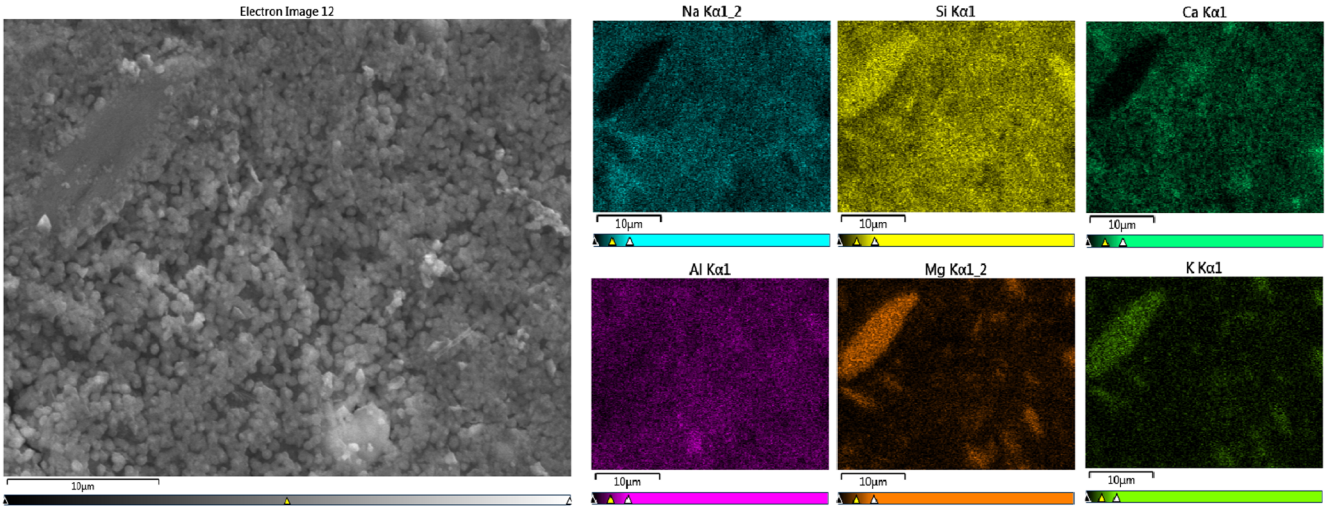

Fig. 7. FESEM secondary electron images and elemental maps for the PM 7/3.

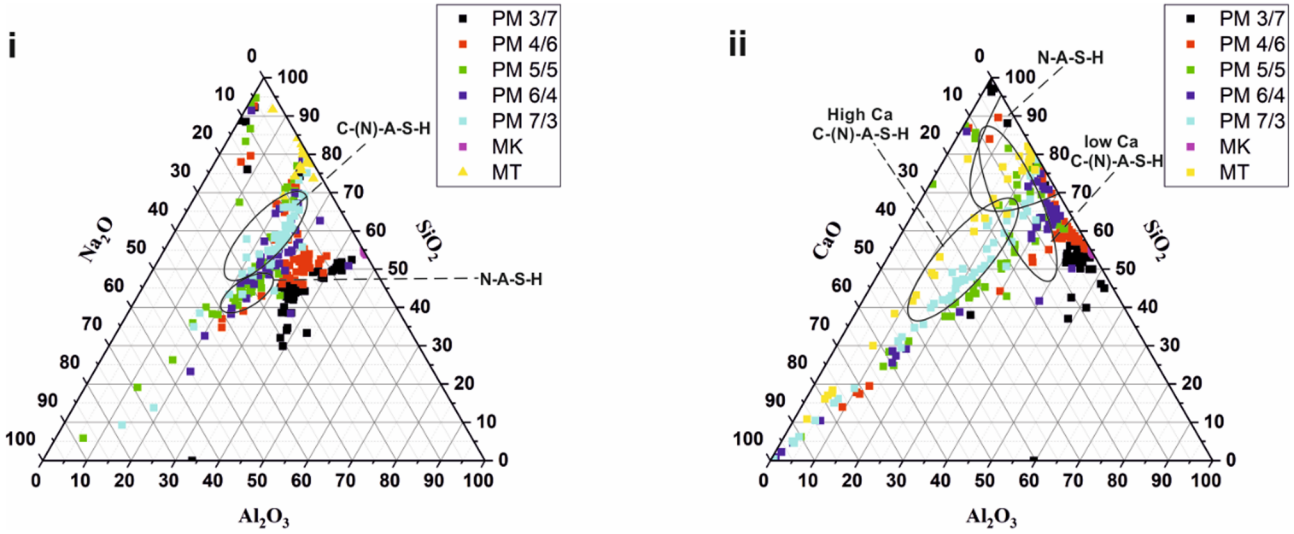

Fig. 8. Projection of alkali-activated materials chemistry onto the i) Na_2O-Al_2O_3-SiO_2 ternary diagram and ii) CaO-Al_2O_3-SiO_2 ternary diagram showing the elemental composition of cured PM samples for 7 days and raw materials. The regions of C-(N)-A-S-H and N-A-S-H were approximately from (Walkley et al., 2016), (Ismail et al., 2014) and (van Deventer et al., 2015).

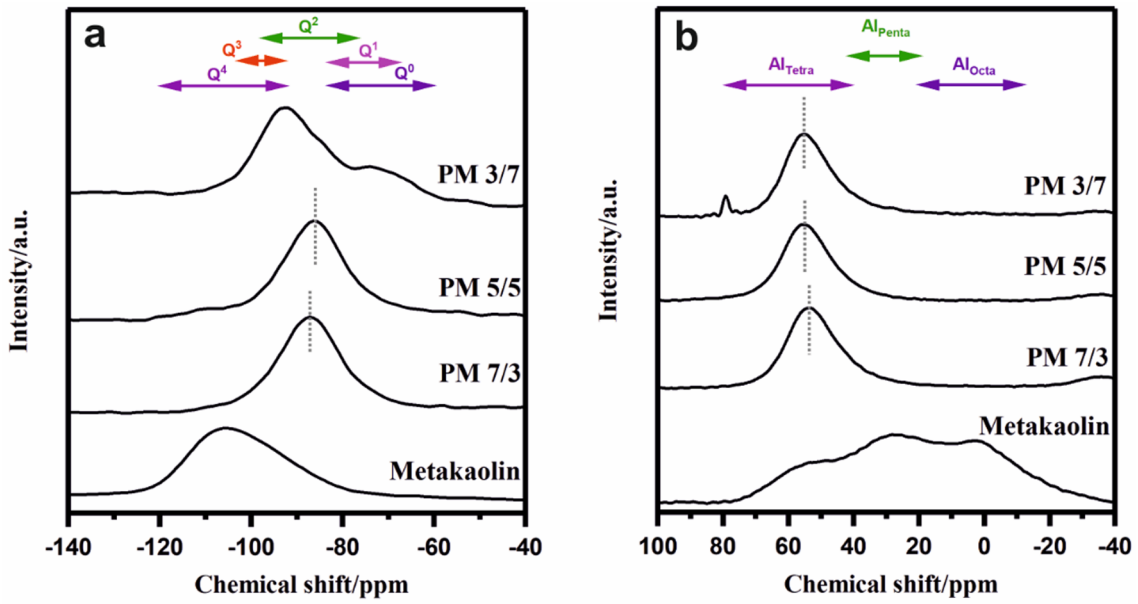

Fig. 9. The results of (a) ^{29}Si NMR and (b) ^{27}Al NMR analysis for products and reactants.

spectrum of MK displayed a broad amorphous component involving mainly Q^4 and Q^3 species. The high strength product, PM 7/3, displayed mainly Q^2 species, which indicated the presence of non-cross-linked C-(N)-A-S-H units. The spectrum of medium strength product PM 5/5 was similar to PM 7/3, except there was a slight shift of the main peak to the right (indicating more non-cross-linked C-(N)-A-S-H phase) and the emergence of a small hump converting Q^4 (indicating N-A-S-H phase) and Q^3 species. In the case of the low-strength sample, PM 3/7, the most dominant feature was a strong peak close to Q^4 (indicating N-A-S-H phase) and Q^3 species. It is possible that Q^3 species formed part of cross-linked C-(N)-A-S-H. Contribution from Q^2 species was a shoulder feature (indicating presence of non-cross-linked C-(N)-A-S-H). Another important feature of this sample is a considerable broad hump covering Q^1 and Q^0 species. This feature indicated the presence of sodium silicate species, which do not contribute to compressive strength like C-(N)-A-S-H. This is one of the reasons for PM3/7 displaying low strength. Both C-(N)-A-S-H and N-A-S-H phase are reported to be formed during alkali activation of clay by-products from phosphate mines (Mabroum et al., 2020).

The results of the ^{27}Al NMR analysis of are depicted in Fig. 9b. MK consists of tetrahedral, pentahedral and octahedral aluminum species. The high-strength product, PM 7/3 consisted tetrahedral aluminum species, which indicated the presence of non-cross-linked C-(N)-A-S-H units. The spectrum of medium strength product PM 5/5 was similar to PM 7/3, except for the slight shift of the tetrahedral peak to the left. In the case of the low strength sample (PM 3/7), a similar tetrahedral component was visible. Notably, C-(N)-A-S-H had tetrahedral aluminum; hence, the spectra of all the products exhibited a similar tetrahedral component. However, there was a small shift of this component towards right as we move from PM 7/3 to PM 3/7. This feature was due to the fact that the chemical shift values of aluminum follows the order: (Al^4 in q^2) > (Al^4 in q^3) > (Al^4 in q^4) (Houston et al., 2009; Myers et al., 2015). The low strength sample PM 3/7 displayed an additional component at approximately 80 ppm which may belong to

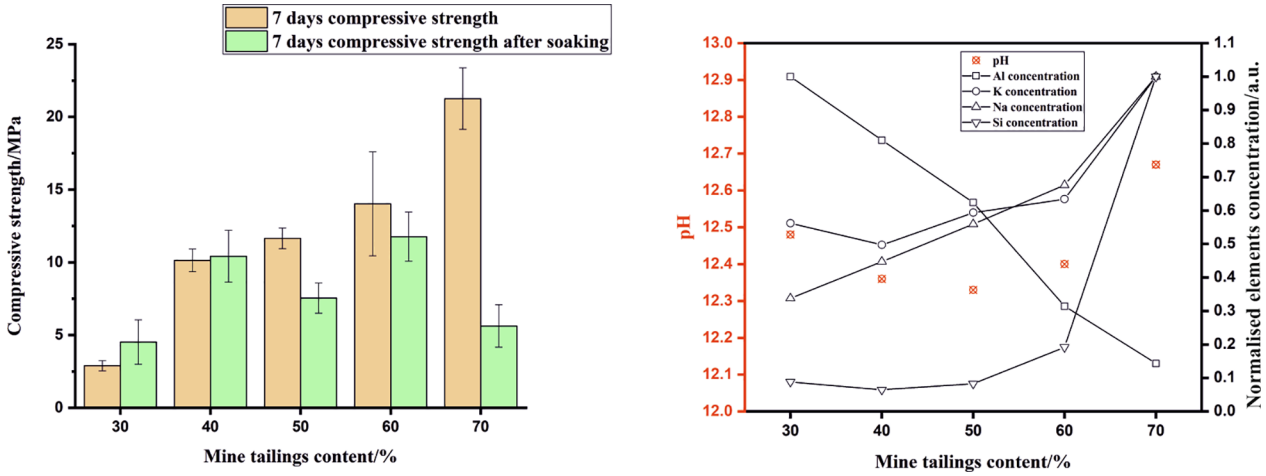

Fig. 10. (a) compressive strength of tailings-metakaolin geopolymer samples after soaking in DI water for 24 h, (b) ICP-OES analysis and pH of the liquid after soaking test.

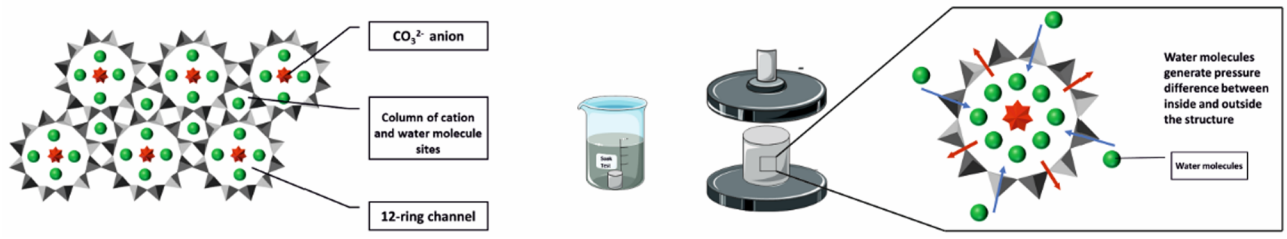

Fig. 11. Schematic structure change of cancrinite after soaking test (aluminosilicate tetrahedra in grey).

low-connectivity aluminate species (Faust and Ribeiro, n.d.; Sagoe-Crentsil and Weng, 2006). Since these species do not contribute to strength-enhancing C-(N)-A-S-H phase, it may contribute towards the low strength of PM 3/7. No octahedral component was detected in any of the products (in spite of having high Mg content), although minor octahedral component corresponding to hydrotalcite is detected in previous study involving alkali activation of clay by-products from phosphate mines (Mabroum et al., 2020).

3.5. Soaking test

The soaking test can affect the UCS of PM samples (Fig. 10), and the decrease of UCS has also been observed in other studies (Boutterin and Davidovits, 2003). There is a synergetic effect between the swelling pressure and regeopolymerization for PM samples. For PM 3/7 and PM 4/6, there is a significant leaching of Al species which means that the geopolymeric reaction was unfulfilled, furthermore, there was less formation of aluminosilicate hydrates indicating a weak and porous matrix. However, dissolvable Al species took part in the re-geopolymerization, which expresses larger effect than swelling repulsion between particles resulting in a higher soaked strength. There is a different situation for PM 5/5, PM 6/4 and PM 7/3, where geopolymerization was achieved thereby the effect of swelling pressure is more conspicuous, leading to a lower strength.

The filtrate was collected and subjected to ICP-OES analysis. The least leaching of sodium concentration in PM 3/7 could be attributed to the strongly bonded sodium cations with negative units such as $Si_4O_8(OH)_6^{4-}$, $SiO(OH)_3^-$ and $SiO_2(OH)_2^{2-}$, forming a rather weak matrix (Panias et al., 2007). Another piece of evidence is the high concentration of Al in solution, indicating a lower amount of aluminium taken part in alkali activation.

As for PM 5/5 and PM 6/4, they consisted of lower amounts of C-(N)-A-S-H gel, revealing the decrease of UCS. It is reasonable to assume that C-(N)-A-S-H gel has higher water-solubility, when compared with N-A-S-H and C-A-S-H gels. Another assumption is that K^+ ions were dissolved from more soluble phases, and this induced capillary force resulting in microcracks within interfaces or grain boundaries.

PM 7/3 had the highest degree of alkali activation and displayed the lowest leaching content of aluminium among all PM samples. Interestingly, it was the sample that was most affected by the 24-h soaking, simultaneously showing the lowest water absorption and porosity (Fig. 1b). These findings might be explained by the presence of cancrinite (Fig. 11). Structural alternation occurred in the cancrinite-like (C-N-A-S-H) gel, in which water can easily penetrate into the cancrinite structure. Cancrinite can be found in nature as a porous mineral, of which the fundamental layers of six-membered rings of SiO_4 and AlO_4 tetrahedra are stacked along the c-axis in an AB-AB sequence (Hackbarth et al., 1999). There are two types of cages within cancrinite structures: 11-hedral cavities and ε-cages along with 12-ring channels as depicted in Fig. 11. The largest discrepancy of UCS in PM 7/3 after soaking might be explained by the structural destabilisation of cancrinite-like (C-N-A-S-H) gel, in which water can easily stab into cancrinite structure. Moreover, the limited space in cages and clogged channels results in the blocking of pore structure, thereby preventing extra water entering. It continues exerting pressure to the porous structure during cage expansion, leading to the low UCS (Liu et al., 2007). Therefore, the weakened alkali-activated structures presented undesirable compressive strength after a 24-h soaking, displaying the lowest water absorption and porosity.

3.6. Life cycle assessment

Fig. 12 shows GWP, AP, EP and ADP (fossil) LCA results for the different alkali-activated binders in comparison to OPC. For the alkali-activated binder (PM 7/3) with the highest UCS (> 20 MPa), excellent performances were shown in impact categories GWP, AP and EP, with 50%, 16% and 18% respectively, lesser emissions than OPC. The significant contributors in these impact categories for PM 7/3 are the

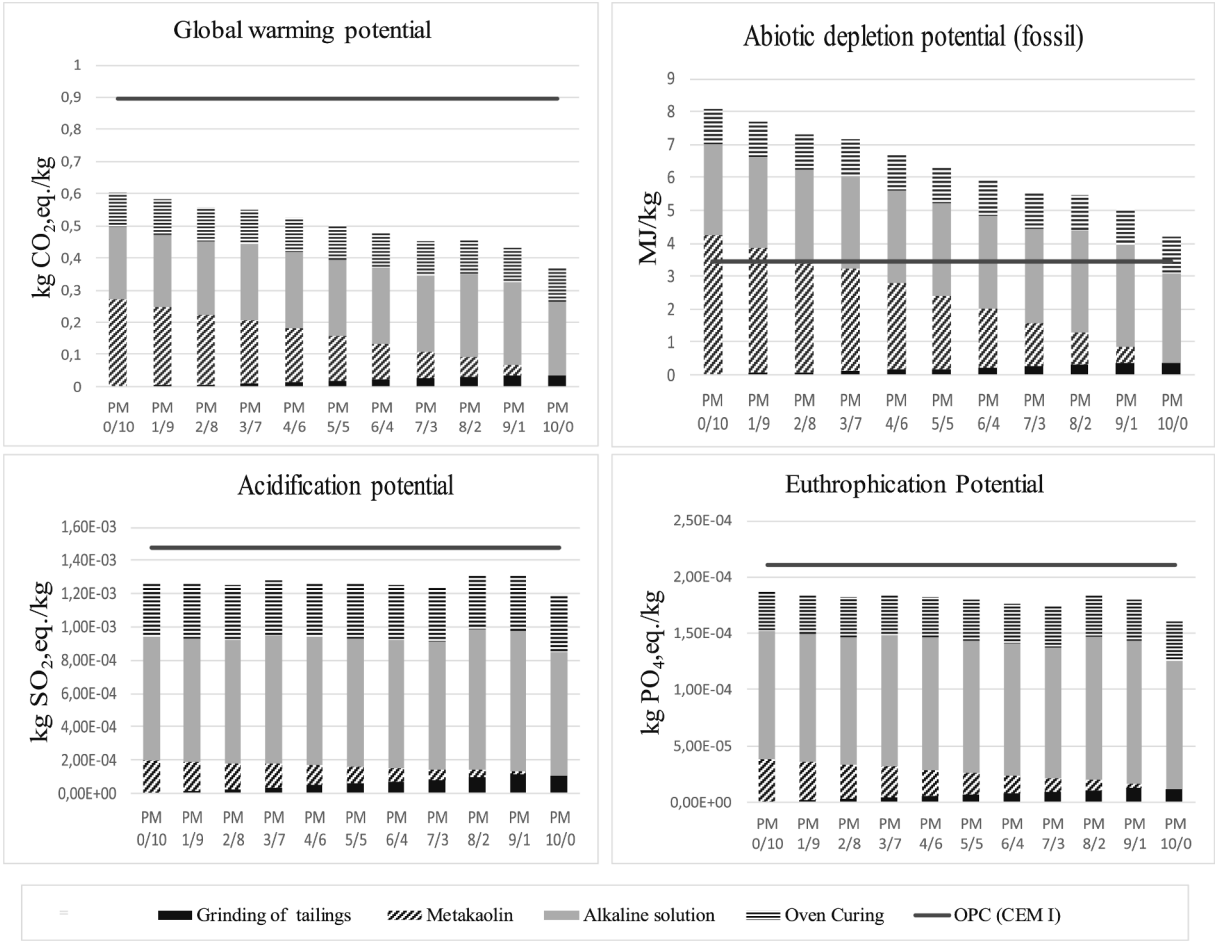

Fig. 12. Life cycle impact assessment results for alkali-activated binder in comparison to CEM I.

alkaline solution (sodium silicate and sodium hydroxide) and curing which account for 52% and 24% respectively for GWP, 62% and 27% respectively for AP, and 67% and 21% for EP. ADP (fossil) showed a significant 61% increase in energy consumption when compared to OPC, with alkaline solution, MK and curing contributing 51%, 24% and 20% respectively. The high amount of energy is associated to energy consumed during production of alkaline solution (Fawer et al., 1999) and in calcining kaolin to MK (Heath et al., 2014). MT beneficiation showed minimal contribution (less than 10%) in all impact categories. This is because only beneficiation impacts were considered, as MT was considered as wastes in this study. Also, MK showed minimal contribution in impact categories AP and EP but a bit higher contribution (19%) in GWP. To reduce the impact of alkaline solution, studies have recommended using silica rich waste materials as a substitute to conventional alkaline solution (Abdulkareem et al., 2019; Passuello et al., 2017). With respect to curing, waste heat can be used for energy thereby increasing the environmental performance of the binder.

As discussed in section 3.1, increasing UCS varies with decreasing apparent porosity and water absorption and when the proportion of MT continuously increases with decrease in MK, the growth of UCS can be seen until it reaches 70% (PM 7/3), at which point it gains the highest UCS > 20 MPa. However, with regards to LCA, continuous increase in MT with decrease in MK leads to a decrease in emissions in GWP, decrease fossil consumption in ADP (fossil) and not much varying effect in AP and EP. This is as a result of MT having lower emissions than MK. It should however be noted that while the UCS of mix designs in this study are considerably lower than that of a standard OPC (32.5 MPa) (BS EN 197–1, 2011). PM 7/3 (> 20 MPa) with 70% MT and 30% MK is closer in strength to OPC. Therefore, improved strength in the mix-design should still amount to lesser emissions compared to OPC.

This LCA study highlights the relevance of using waste materials in the development of alkali-activated binders. Not only are significant impact reductions achieved, but a useful alternative to simply disposing waste residues (which may eventually lead to contamination) is provided.

4. Conclusion

This study investigated the synthesis of AAM using mechanochemically activated phosphate MT with MK as (calcium) aluminosilicate precursors. The geopolymer with the higher content of tailings (60% to 70%) displayed the best mechanical properties (> 20 MPa).

There were two main factors to consider: 1) The mechanochemical activation improves the chemical reactivity of tailings, and 2) the presence of calcium-rich carbonate minerals accelerates the formation of C-(N)-A-S-H binder. The chemical process of alkali-activated phosphate tailings-metakaolin based geopolymers appear to more complicated due to the appearance of the C-(N)-A-S-H binder. New zeolites, such as natrolite (which was fibre-like) and cancrinite (which was column-like) formed.

With the increment of tailings quantity (> 70%), water requirement was lowered due to more favourable particle shape. Although the highest compressive strength was achieved with 70% tailings, water resistance in PM 7/3 still required further improvement. The recycling of MT significantly depends on its chemical and mineralogical composition, and its interactions with alkaline activators.

From the view of circular economy, this study provides a potential method to recycle mine tailings with high added value rather than backfill or impoundment. The manufacturing of tailings-based geopolymers gives huge opportunities for local availability such as

minimizing traffic expense and maximizing sustainability. Particularly, it considerably decreases CO_2 emissions in comparison with OPC. According to the performance of tailings-based geopolymers, such a material displayed promising properties for construction applications, such as brick manufacturing.

CRediT authorship contribution statement

He Niu: Writing - original draft, Conceptualization, Formal analysis. **Mariam Abdulkareem:** Writing - original draft. **Harisankar Sreenivasan:** Writing - original draft. **Anu M. Kantola:** Writing - original draft. **Jouni Havukainen:** Writing - original draft. **Mika Horttanainen:** Writing - original draft. **Ville-Veikko Telkki:** Writing - original draft. **Paivo Kinnunen:** Conceptualization, Supervision, Writing - review & editing. **Mirja Illikainen:** Supervision, Writing - review & editing, Funding acquisition.

Declaration of Competing Interest

The authors declare that they have no known competing financial interests or personal relationships that could have appeared to influence the work reported in this paper.

Acknowledgement

The authors gratefully acknowledge the financial support from the Academy of Finland [grants #292526, #319676 and #326291] and the European Union's EU Framework Programme for Research and Innovation Horizon 2020 [Grant Agreement No 812580 ("SULTAN", https://etn-sultan.eu)]. The authors would like to thank Pasi Juntunen for the assistance in FESEM measurement, Mr. Pekka Tanskanen and Mr. Marcin Selent for their assistance in XRD analysis, Mr. Aki-Petteri Pokka for the assistance in compressive strength measurement. Mr. Jarno Karvonen and Mr. Jani Österlund are acknowledged for their contribution in laboratory experiments. V.-V.T. thanks the Academy of Finland (grants #289649, 294027 and 319216) for the financial support.

Appendix A. . Fundamental information of precursors

See Figs. A1 and A2 Table A1.

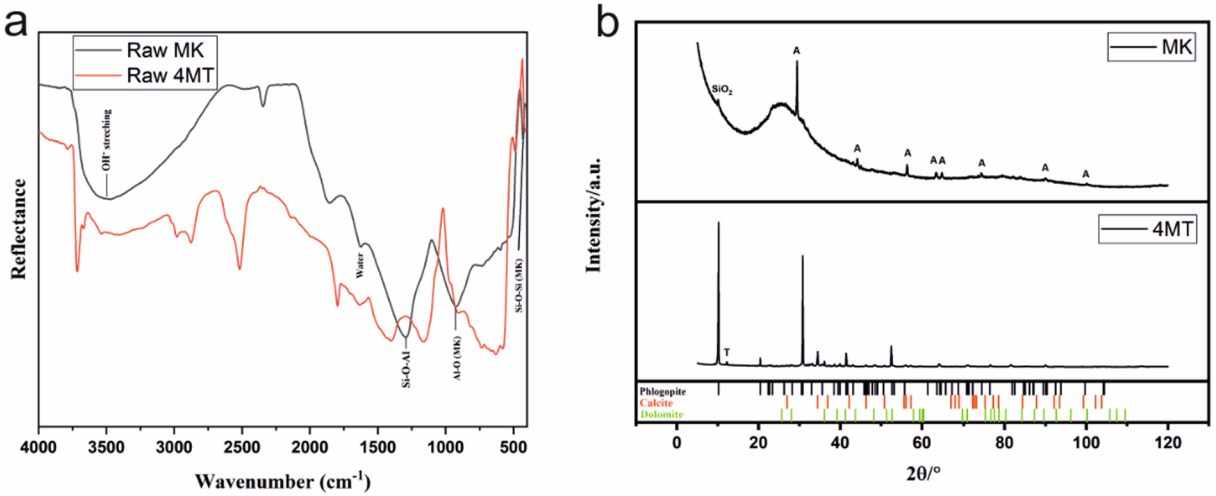

Fig. A1. (a) DRIFT spactra of raw materials (b) XRD patterns of raw materials. quartz (#04-007-2627), A: anatase (#00-064-0803), T: tremolite (#04-013-2249).

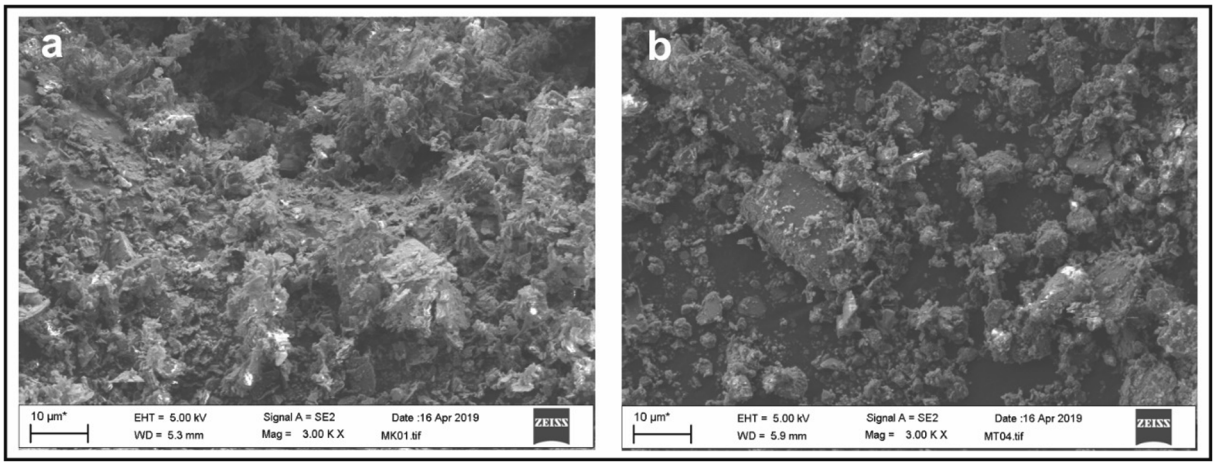

Fig. A2. (a) SEM secondary electron micrographs of metakaolin, (b) SEM secondary electron micrographs of 4-min ground phosphate mine tailings.

Table A1
Description of main bands of 4-min ground phosphate mine tailings.

Wavenumber (cm^{-1})	Band characterization	Reference
3711	OH-stretching vibration (phlogopite)	(Bigham et al., 2001; Farmer, 1974; Schingaro et al., 2013)
3665	OH-stretching vibration Group I (tremolite)	(Najorka and Gottschalk, 2003)
3535	OH-stretching vibration Group III (tremolite)	(Najorka and Gottschalk, 2003)
2979	Carbonate ν_2 overtone (dolomite)	(Messerschmidt, 1985; Nguyen et al., 1991)
2873	Carbonate (calcite)	(Messerschmidt, 1985; Nguyen et al., 1991)
2519	$2\nu_2 + \nu_4$ combination mode (dolomite, calcite)	(Gunasekaran and Anbalagan, n.d.; Nguyen et al., 1991)
1795	Carbonate (calcite)	(Nguyen et al., 1991)
1635	Carbonate ν_3 (apatite)	(Bigham et al., 2001; Rehman and Bonfield, 1997)
1395	C-O Asymmetric stretching ν_3 (dolomite, calcite)	(Clark, n.d.)
1162	Si-O-T (T: Si or Al) (phlogopite)	(Rees et al., 2007)
974	Non-diagnostic Si-O stretching (phlogopite)	(Bigham et al., 2001; Farmer, 1974)
905	Out-of-plane bending ν_2 (dolomite, calcite)	(Farmer, 1974; Rehman and Bonfield, 1997)
823	Apical Al-O bond from AlO_4 (phlogopite)	(Bigham et al., 2001; Farmer, 1974)
732	In-plane bending ν_4 (dolomite, calcite)	(Gunasekaran and Anbalagan, n.d.)
693	Perpendicular vibration (phlogopite)	(Bigham et al., 2001; Farmer, 1974)
665	In-plane vibration of Al-O-Si (phlogopite)	(Bigham et al., 2001; Farmer, 1974)
628	OH vibration (phlogopite)	(Bigham et al., 2001; Farmer, 1974)
579	Asymmetric deformation ν_4 (apatite)	(Veiderma et al., 1998)

Appendix B. . Data sources for Life cycle inventory

See Table B1.

Table B1
Data sources.

Type of data	Source
Sodium hydroxide	GaBi database 2019 (EU-28, sodium hydroxide, 100% caustic soda)
Sodium silicate solution	(Fawer et al., 1999) (sodium silicate 3.3, furnace liquor, 37% solid)
Cement	(CEMBUREAU, 2015) (OPC CEM I)
Metakaolin	Heath et al., 2014; NLK, 2002
Water	GaBi database, 2019 (EU- 28, tap water)
Electricity	GaBi database, 2019 (Finland, electricity grid mix)

References

Abdulkareem, M., Havukainen, J., Horttanainen, M., 2019. How environmentally sustainable are fibre reinforced alkali-activated concretes? J. Clean. Prod. 236. https://doi.org/10.1016/J.JCLEPRO.2019.07.076.

Ahmari, S., Zhang, L., 2013. Utilization of cement kiln dust (CKD) to enhance mine tailings-based geopolymer bricks. Constr. Build. Mater. 40, 1002–1011. https://doi.org/10.1016/j.conbuildmat.2012.11.069.

Alonso, Santiago, Palomo, A., 2001a. Calorimetric study of alkaline activation of calcium hydroxide–metakaolin solid mixtures. Cem. Concr. Res. 31, 25–30. https://doi.org/10.1016/S0008-8846(00)00435-X.

Alonso, S., Palomo, A., 2001b. Alkaline activation of metakaolin and calcium hydroxide mixtures: influence of temperature, activator concentration and solids ratio. Mater. Lett. 47, 55–62. https://doi.org/10.1016/S0167-577X(00)00212-3.

Bakharev, T., 2005. Resistance of geopolymer materials to acid attack. Cem. Concr. Res. 35, 658–670.

Balczár, I., Korim, T., Kovács, A., Makó, É., 2016. Mechanochemical and thermal activation of kaolin for manufacturing geopolymer mortars–Comparative study. Ceram. Int. 42, 15367–15375.

Bigham, J.M., Bhatti, T.M., Vuorinen, A., Tuovinen, O.H., 2001. Dissolution and structural alteration of phlogopite mediated by proton attack and bacterial oxidation of ferrous iron. Hydrometallurgy 59, 301–309. https://doi.org/10.1016/S0304-386X(00)00186-9.

Boldyreva, E., 2013. Mechanochemistry of inorganic and organic systems: what is similar, what is different? Chem. Soc. Rev. 42, 7719. https://doi.org/10.1039/c3cs60052a.

Bouaissi, A., 2019. Mechanical properties and microstructure analysis of FA-GGBS-HMNS based geopolymer concrete. Constr. Build. Mater. 12.

Boutterin, C., Davidovits, J., 2003. Réticulation géopolymérique (LTGS) et matériaux de construction. Géopolymère 1, 79–88.

CEMBUREAU, 2015. Environmental Product Declaration (EPD) Portland Cement (CEM I) produced in Europe.

Chen, C., Habert, G., Bouzidi, Y., Jullien, A., 2010a. Environmental impact of cement production: detail of the different processes and cement plant variability evaluation. J. Clean. Prod. 18, 478–485. https://doi.org/10.1016/j.jclepro.2009.12.014.

Chen, S., Wu, M., Zhang, S., 2010b. Mineral phases and properties of alkali-activated metakaolin-slag hydroceramics for a disposal of simulated highly-alkaline wastes. J. Nucl. Mater. 402, 173–178. https://doi.org/10.1016/j.jnucmat.2010.05.015.

Chindaprasirt, P., Jaturapitakkul, C., Chalee, W., Rattanasak, U., 2009. Comparative study on the characteristics of fly ash and bottom ash geopolymers. Waste Manag. 29, 539–543. https://doi.org/10.1016/j.wasman.2008.06.023.

Clark, R.N., n.d. Spectroscopy of Rocks and Minerals, and Principles of Spectroscopy 64.

Criado, M., Fernández-Jiménez, A., de la Torre, A.G., Aranda, M.A.G., Palomo, A., 2007. An XRD study of the effect of the SiO2/Na2O ratio on the alkali activation of fly ash. Cem. Concr. Res. 37, 671–679. https://doi.org/10.1016/j.cemconres.2007.01.013.

Duxson, P., Provis, J.L., Lukey, G.C., van Deventer, J.S.J., 2007. The role of inorganic polymer technology in the development of 'green concrete'. Cem. Concr. Res. 37, 1590–1597. https://doi.org/10.1016/j.cemconres.2007.08.018.

El Hafid, K., Hajjaji, M., 2015. Effects of the experimental factors on the microstructure and the properties of cured alkali-activated heated clay. Appl. Clay Sci. 116–117, 202–210. https://doi.org/10.1016/j.clay.2015.03.015.

EN ISO 14040, 2006. SFS-EN ISO 14040 ENVIRONMENTAL MANAGEMENT. LIFE CYCLE ASSESSMENT . PRINCIPLES AND FRAME- WORK (ISO 14040 : 2006).

EN, T., 2007. Natural stone test methods-Determination of real density and apparent density, and of total and open porosity. Turk. Stand. Inst. Ank. 13.

Farmer, V.C., 1974. Infrared spectra of minerals. Mineralogical society.

Faust, B.C., Ribeiro, A., n.d. Speciation of aqueous mononuclear AI(III)-hydroxo and other AI (III) complexes at concentrations of geochemical relevance by aluminum-27 nuclear magnetic resonance spectroscopy 11.

Fawer, M., Concannon, M., Rieber, W., 1999. Life cycle inventories for the production of sodium silicates. Int. J. Life Cycle Assess. 4, 207–212. https://doi.org/10.1007/BF02979498.

Fernández-Jiménez, A., Palomo, A., 2005. Mid-infrared spectroscopic studies of alkali-activated fly ash structure. Microporous Mesoporous Mater. 86, 207–214. https://doi.org/10.1016/j.micromeso.2005.05.057.

J.A. Gadsden, Infrared spectra of minerals and related inorganic compounds, 1975.

García-Lodeiro, I., Fernández-Jiménez, A., Blanco, M.T., Palomo, A., 2008. FTIR study of

the sol–gel synthesis of cementitious gels: C-S–H and N–A–S–H. J. Sol-Gel Sci. Technol. 45, 63–72. https://doi.org/10.1007/s10971-007-1643-6.
García-Lodeiro, I., Fernández-Jiménez, A., Palomo, A., Macphee, D.E., 2010. Effect of calcium additions on N-A-S-H cementitious gels. J. Am. Ceram. Soc. https://doi.org/10.1111/j.1551-2916.2010.03668.x.
Garcia-Lodeiro, I., Palomo, A., Fernández-Jiménez, A., Macphee, D.E., 2011. Compatibility studies between N-A-S-H and C-A-S-H gels. Study in the ternary diagram Na_2O–CaO–Al_2O_3–SiO_2–H_2O. Cem. Concr. Res. 41, 923–931. https://doi.org/10.1016/j.cemconres.2011.05.006.
Gunasekaran, S., Anbalagan, G., n.d. Thermal decomposition of natural dolomite 6.
Hackbarth, K., Gesing, T.M., Fechtelkord, M., Stief, F., 1999. Synthesis and crystal structure of carbonate cancrinite $Na_8[AlSiO_4]_6CO_3(H_2O)_{3.4}$, grown under low-temperature hydrothermal conditions. Microporous Mesoporous Mater. 12.
Hasanbeigi, A., Menke, C., Price, L., 2010. The CO_2 abatement cost curve for the Thailand cement industry. J. Clean. Prod. 18, 1509–1518. https://doi.org/10.1016/j.jclepro.2010.06.005.
Heath, A., Paine, K., McManus, M., 2014. Minimising the global warming potential of clay based geopolymers. J. Clean. Prod. 78, 75–83. https://doi.org/10.1016/j.jclepro.2014.04.046.
Houston, J.R., Maxwell, R.S., Carroll, S.A., 2009. Transformation of meta-stable calcium silicate hydrates to tobermorite: reaction kinetics and molecular structure from XRD and NMR spectroscopy. Geochem. Trans. 10, 1. https://doi.org/10.1186/1467-4866-10-1.
Huang, X., Huang, T., Li, S., Muhammad, F., Xu, G., Zhao, Z., Yu, L., Yan, Y., Li, D., Jiao, B., 2016. Immobilization of chromite ore processing residue with alkali-activated blast furnace slag-based geopolymer. Ceram. Int. 42, 9538–9549. https://doi.org/10.1016/j.ceramint.2016.03.033.
Ismail, I., Bernal, S.A., Provis, J.L., San Nicolas, R., Hamdan, S., van Deventer, J.S.J., 2014. Modification of phase evolution in alkali-activated blast furnace slag by the incorporation of fly ash. Cem. Concr. Compos. 45, 125–135. https://doi.org/10.1016/j.cemconcomp.2013.09.006.
Johnson, C.D., Worrall, F., 2007. Novel low density granular adsorbents – properties of a composite matrix from zeolitisation of vermiculite. Chemosphere 68, 1153–1162. https://doi.org/10.1016/j.chemosphere.2007.01.049.
Kauppila, P., Räsänen, M.L., Myllyoja, S., 2013. Best Environmental Practices in Metal Ore Mining (Metallimalmikaivostoiminnan parhaat ympäristökäytännöt).
Kinnunen, P., Ismailov, A., Solismaa, S., Sreenivasan, H., Räisänen, M.-L., Levänen, E., Illikainen, M., 2018. Recycling mine tailings in chemically bonded ceramics – a review. J. Clean. Prod. 174, 634–649. https://doi.org/10.1016/j.jclepro.2017.10.280.
M. Król, P. Rożek, W. Mozgawa, Preparation and Structure of Geopolymer-Based Alkali-Activated Circulating Fuildized Bed Ash Composite for Removing Ni2+ from Wastewater, in: D. Singh, M. Fukushima, Y.-W. Kim, K. Shimamura, N. Imanaka, T. Ohji, J. Amoroso, M. Lanagan (Eds.), Ceram. Trans. Ser., John Wiley & Sons, Inc., Hoboken, NJ, USA, 2018: pp. 147–154. doi:10.1002/9781119494096.ch15.
Liu, Q., Navrotsky, A., Jove-Colon, C.F., Bonhomme, F., 2007. Energetics of cancrinite: effect of salt inclusion. Microporous Mesoporous Mater. 98, 227–233. https://doi.org/10.1016/j.micromeso.2006.09.008.
Mabroum, S., Aboulayt, A., Taha, Y., Benzaazoua, M., Semlal, N., Hakkou, R., 2020. Elaboration of geopolymers based on clays by-products from phosphate mines for construction applications. J. Clean. Prod. 261, 121317. https://doi.org/10.1016/j.jclepro.2020.121317.
MacKenzie, K.J.D., Brew, D.R.M., Fletcher, R.A., Vagana, R., 2007. Formation of aluminosilicate geopolymers from 1:1 layer-lattice minerals pre-treated by various methods: a comparative study. J. Mater. Sci. 42, 4667–4674. https://doi.org/10.1007/s10853-006-0173-x.
Maragkos, I., Giannopoulou, I.P., Panias, D., 2009. Synthesis of ferronickel slag-based geopolymers. Miner. Eng. 22, 196–203. https://doi.org/10.1016/j.mineng.2008.07.003.
Merrild, H., Larsen, A.W., Christensen, T.H., 2012. Assessing recycling versus incineration of key materials in municipal waste: the importance of efficient energy recovery and transport distances. Waste Manage. 32, 1009–1018. https://doi.org/10.1016/J.WASMAN.2011.12.025.
Messerschmidt, R.G., 1985. Complete elimination of specular reflectance in infrared diffuse reflectance measurements. Appl. Spectrosc. 39, 737–739. https://doi.org/10.1366/0003702854250167.
Mladenovič, A., Šuput, J.S., Ducman, V., Škapin, A.S., 2004. Alkali–silica reactivity of some frequently used lightweight aggregates. Cem. Concr. Res. 34, 1809–1816. https://doi.org/10.1016/j.cemconres.2004.01.017.
Mo, B., Zhu, H., Cui, X., He, Y., Gong, S., 2014. Effect of curing temperature on geopolymerization of metakaolin-based geopolymers. Appl. Clay Sci. 99, 144–148. https://doi.org/10.1016/j.clay.2014.06.024.
Moukannaa, S., Loutou, M., Benzaazoua, M., Vitola, L., Alami, J., Hakkou, R., 2018. Recycling of phosphate mine tailings for the production of geopolymers. J. Clean. Prod. 185, 891–903. https://doi.org/10.1016/j.jclepro.2018.03.094.
Moukannaa, S., Nazari, A., Bagheri, A., Loutou, M., Sanjayan, J.G., Hakkou, R., 2019. Alkaline fused phosphate mine tailings for geopolymer mortar synthesis: Thermal stability, mechanical and microstructural properties. J. Non-Cryst. Solids 511, 76–85. https://doi.org/10.1016/j.jnoncrysol.2018.12.031.
Mozgawa, W., 2001. The relation between structure and vibrational spectra of natural zeolites. J. Mol. Struct. 596, 129–137. https://doi.org/10.1016/S0022-2860(01)00741-4.
Mucsi, G., Kumar, S., Csőke, B., Kumar, R., Molnár, Z., Rácz, Á., Mádai, F., Debreczeni, Á., 2015. Control of geopolymer properties by grinding of land filled fly ash. Int. J. Miner. Process. 143, 50–58. https://doi.org/10.1016/j.minpro.2015.08.010.
Myers, R.J., Bernal, S.A., Gehman, J.D., van Deventer, J.S.J., Provis, J.L., 2015. The role of Al in cross-linking of alkali-activated slag cements. J. Am. Ceram. Soc. 98, 996–1004. https://doi.org/10.1111/jace.13360.
Najorka, J., Gottschalk, M., 2003. Crystal chemistry of tremolite-tschermakite solid solutions. Phys. Chem. Miner. 30, 108–124. https://doi.org/10.1007/s00269-002-0291-1.
Nguyen, T., Janik, L., Raupach, M., 1991. Diffuse reflectance infrared fourier transform (DRIFT) spectroscopy in soil studies. Soil Res. 29, 49. https://doi.org/10.1071/SR9910049.
Niu, H., Kinnunen, P., Sreenivasan, H., Adesanya, E., Illikainen, M., 2020. Structural collapse in phlogopite mica-rich mine tailings induced by mechanochemical treatment and implications to alkali activation potential. Miner. Eng. 151, 106331. https://doi.org/10.1016/j.mineng.2020.106331.
NLK, 2002. Ecosmart concrete project: Metakaolin Pre-feasibility study, Report EA2860. Vancouver, British Columbia.
Novais, R.M., Ascensão, G., Tobaldi, D.M., Seabra, M.P., Labrincha, J.A., 2018. Biomass fly ash geopolymer monoliths for effective methylene blue removal from wastewaters. J. Clean. Prod. 171, 783–794.
O'Brien, H., Heilimo, E., Heino, P., 2015. Chapter 4.3 - The Archean Siilinjärvi Carbonatite Complex, in: Maier, W.D., Lahtinen, R., O'Brien, Hugh (Eds.), Mineral Deposits of Finland. Elsevier, pp. 327–343. https://doi.org/10.1016/B978-0-12-410438-9.00013-3.
Oelkers, E.H., Gislason, S.R., 2001. The mechanism, rates and consequences of basaltic glass dissolution: I. An experimental study of the dissolution rates of basaltic glass as a function of aqueous Al, Si and oxalic acid concentration at 25°C and pH = 3 and 11. Geochim. Cosmochim. Acta 65, 3671–3681. https://doi.org/10.1016/S0016-7037(01)00664-0.
Palomo, A., Glasser, F., 1992. Chemically-bonded cementitious materials based on metakaolin. Br. Ceram. Trans. J. 91, 107–112.
Panias, D., Giannopoulou, I.P., Perraki, T., 2007. Effect of synthesis parameters on the mechanical properties of fly ash-based geopolymers. Colloids Surf. Physicochem. Eng. Asp. 301, 246–254. https://doi.org/10.1016/j.colsurfa.2006.12.064.
Passuello, A., Rodríguez, E.D., Hirt, E., Longhi, M., Bernal, S.A., Provis, J.L., Kirchheim, A.P., 2017. Evaluation of the potential improvement in the environmental footprint of geopolymers using waste-derived activators. J. Clean. Prod. 166, 680–689. https://doi.org/10.1016/j.jclepro.2017.08.007.
Petrillo, A., Cioffi, R., De Felice, F., Colangelo, F., Borrelli, C., 2016. An environmental evaluation: a comparison between geopolymer and OPC concrete paving blocks manufacturing process in italy. Environ. Prog. Sustain. Energy 35, 1699–1708. https://doi.org/10.1002/ep.12421.
Provis, J., 2013. Alkali activated materials: state-of-the-art report, RILEM TC 224-AAM. Springer, New York.
Rattanasak, U., Chindaprasirt, P., 2009. Influence of NaOH solution on the synthesis of fly ash geopolymer. Miner. Eng. 22, 1073–1078. https://doi.org/10.1016/j.mineng.2009.03.022.
Rees, C.A., Provis, J.L., Lukey, G.C., van Deventer, J.S.J., 2007. In situ ATR-FTIR study of the early stages of fly ash geopolymer gel formation. Langmuir 23, 9076–9082. https://doi.org/10.1021/la701185g.
Rehman, I., Bonfield, W., 1997. Characterization of hydroxyapatite and carbonated apatite by photo acoustic FTIR spectroscopy. J. Mater. Sci. Mater. Med. 8, 1–4. https://doi.org/10.1023/A:1018570213546.
Sagoe-Crentsil, K., Weng, L., 2006. Dissolution processes, hydrolysis and condensation reactions during geopolymer synthesis: Part II. High Si/Al ratio systems. J. Mater. Sci. 42, 3007–3014. https://doi.org/10.1007/s10853-006-0818-9.
Schingaro, E., Lacalamita, M., Scordari, F., Mesto, E., 2013. 3T-phlogopite from Kasenyi kamafugite (SW Uganda): EPMA, XPS, FTIR, and SCXRD study. Am. Mineral. 98, 709–717. https://doi.org/10.2138/am.2013.4283.
Slaty, F., Khoury, H., Rahier, H., Wastiels, J., 2015. Durability of alkali activated cement produced from kaolinitic clay. Appl. Clay Sci. 104, 229–237. https://doi.org/10.1016/j.clay.2014.11.037.
Smith Aitken, W.W., 1965. An occurrence of phlogopite and its transformation to vermiculite by weathering. Mineral. Mag. J. Mineral. Soc. 35, 151–164. https://doi.org/10.1180/minmag.1965.035.269.18.
Thinkstep, 2019. Description of the CML 2001 method [WWW Document]. URL http://www.gabi-software.com/support/gabi/gabi-lcia-documentation/cml-2001/ (accessed 6.30.19).
Valentini, L., Contessi, S., Dalconi, M.C., Zorzi, F., Garbin, E., 2018. Alkali-activated calcined smectite clay blended with waste calcium carbonate as a low-carbon binder. J. Clean. Prod. 184, 41–49. https://doi.org/10.1016/j.jclepro.2018.02.249.
Van Den Heede, P., De Belie, N., 2012. Environmental impact and life cycle assessment (LCA) of traditional and "green" concretes: Literature review and theoretical calculations. Cem. Concr. Compos. 34, 431–442. https://doi.org/10.1016/j.cemconcomp.2012.01.004.
van Deventer, J.S.J., San Nicolas, R., Ismail, I., Bernal, S.A., Brice, D.G., Provis, J.L., 2015. Microstructure and durability of alkali-activated materials as key parameters for standardization. J. Sustain. Cem.-Based Mater. 4, 116–128. https://doi.org/10.1080/21650373.2014.979265.
Veiderma, M., Knubovets, R., Tõnsuaadu, K., 1998. Structural properties of apatites from Finland studied by FTIR spectroscopy. Bull. Geol. Soc. Finl. 70, 69–75. https://doi.org/10.17741/bgsf/70.1-2.005.
Vickers, L., van Riessen, A., Rickard, W.D.A., 2015. Fire-Resistant Geopolymers, SpringerBriefs in Materials. Springer Singapore, Singapore. https://doi.org/10.1007/978-981-287-311-8.
Walkley, B., San Nicolas, R., Sani, M.-A., Rees, G.J., Hanna, J.V., van Deventer, J.S.J., Provis, J.L., 2016. Phase evolution of C-(N)-A-S-H/N-A-S-H gel blends investigated via alkali-activation of synthetic calcium aluminosilicate precursors. Cem. Concr. Res. 89, 120–135. https://doi.org/10.1016/j.cemconres.2016.08.010.
Wei, B., Zhang, Y., Bao, S., 2017. Preparation of geopolymers from vanadium tailings by

mechanical activation. Constr. Build. Mater. 145, 236–242. https://doi.org/10.1016/j.conbuildmat.2017.03.234.
Ye, J., Zhang, W., Shi, D., 2014a. Effect of elevated temperature on the properties of geopolymer synthesized from calcined ore-dressing tailing of bauxite and ground-granulated blast furnace slag. Constr. Build. Mater. 69, 41–48. https://doi.org/10.1016/j.conbuildmat.2014.07.002.
Ye, N., Yang, J., Ke, X., Zhu, J., Li, Y., Xiang, C., Wang, H., Li, L., Xiao, B., 2014b. Synthesis and characterization of geopolymer from bayer red mud with thermal pretreatment. J. Am. Ceram. Soc. 97, 1652–1660. https://doi.org/10.1111/jace.12840.
Yip, C.K., Lukey, G.C., van Deventer, J.S.J., 2005. The coexistence of geopolymeric gel and calcium silicate hydrate at the early stage of alkaline activation. Cem. Concr. Res. 35, 1688–1697. https://doi.org/10.1016/j.cemconres.2004.10.042.
Zhang, L., 2013. Production of bricks from waste materials – a review. Constr. Build. Mater. 47, 643–655. https://doi.org/10.1016/j.conbuildmat.2013.05.043.